

Synthetic-Aperture Radar Processing Using Fast Factorized Back-Projection

LARS M. H. ULANDER, Member, IEEE

HANS HELLSTEN

GUNNAR STENSTRÖM

Swedish Defence Research Agency (FOI)

Exact synthetic aperture radar (SAR) inversion for a linear aperture may be obtained using fast transform techniques. Alternatively, back-projection integration in time domain can also be used. This technique has the benefit of handling a general aperture geometry. In the past, however, back-projection has seldom been used due to heavy computational burden. We show that the back-projection integral can be recursively partitioned and an effective algorithm constructed based on aperture factorization. By representing images in local polar coordinates it is shown that the number of operations is drastically reduced and can be made to approach that of fast transform algorithms. The algorithm is applied to data from the airborne ultra-wideband CARABAS SAR and shown to give a reduction in processing time of two to three orders of magnitude.

Manuscript received December 13, 2000; revised June 27 and November 19, 2002; released for publication March 13, 2003.

IEEE Log No. T-AES/39/3/816615.

Refereeing of this contribution was handled by L. M. Kaplan.

Authors' current addresses: L. M. H. Ulander, Swedish Defence Research Agency (FOI), PO Box 1165, SE-581 11, Linköping, Sweden, E-mail: (ulander@foi.se); H. Hellsten, Ericsson Microwave Systems, Sweden; G. Stenström, Swedish Defence Research Agency (FOI), Division of Sensor Technology, Dept. of Radar Systems, PO Box 1165, SE-581 11 Linköping, Sweden.

0018-9251/03/\$17.00 © 2003 IEEE

I. INTRODUCTION

Synthetic aperture radar (SAR) is a general method for generating high-resolution radar maps from low-resolution aperture data which is based on using the relative motion between the radar antenna and the imaged scene. Originally conceived in the early 1950s [1], it is extensively used to image objects on the surface of the Earth and the planets [2]. A synthetic aperture is formed using electromagnetic signals from a physical aperture located at different space-time positions. The synthetic aperture may therefore observe the scene over a large angular sector by moving the physical aperture. Hence, the technique can give a significant improvement in resolution, in principle limited only by the stability of the wave field and other restrictions imposed on the movement of the physical aperture. A physical aperture, on the other hand, provides angular resolution inversely proportional to aperture size such that the spatial resolution degrades with increasing distance to the scene.

SAR images of the ground are often generated from pulse echo data acquired by an antenna moving along a nominally linear track. It is well known that the spatial resolution can be made independent of distance to the ground since the antenna can be moved along correspondingly longer tracks [2]. It is therefore possible to produce radar maps with meter- or decimeter-resolution from aircraft or spacecraft at very large distances. The resolution in these systems are limited by antenna illumination and system bandwidth but also by other factors, e.g. accuracy of antenna positioning, propagation perturbations, transmitter power, receiver sensitivity, clock stability, and dynamic range.

The ultimate limit of SAR spatial resolution is proportional to the wavelength. The finest resolution is determined by the classical uncertainty principle applied to a band-limited wave packet. The area of a resolution cell can be shown to be related to radar system bandwidth B ($= f_{\max} - f_{\min}$, where f_{\max} and f_{\min} are the maximum and minimum electromagnetic frequency, respectively) and aperture angle $\vartheta_2 - \vartheta_1$ (the angle over which the antenna is moved and radiating as seen from the imaged ground) according to [3]

$$\Delta A_{\text{SAR}} = \frac{\lambda_c}{2(\vartheta_2 - \vartheta_1)} \frac{c}{2B} \quad (1)$$

where λ_c is the wavelength corresponding to the center frequency, i.e. $\lambda_c = c/f_c$, where $f_c = (f_{\max} + f_{\min})/2$, and c is the speed of light. Finer resolution is therefore achieved by increasing B and $\vartheta_2 - \vartheta_1$, or by decreasing λ_c . The system transfer function is shown in Fig. 1 which has the form of a sector of a circular annulus in wavenumber domain. The sector is defined by the aperture angle, whereas the annulus is defined by the center frequency and bandwidth. The

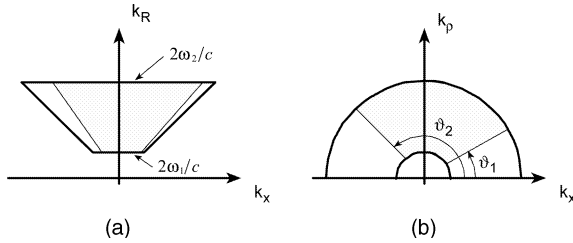


Fig. 1. System transfer function before (a) and after (b) SAR processing. Radial, along-track, across-track wavenumbers are denoted k_R , k_x , k_p . Area in wavenumber domain is radar signal support for a target illuminated by bandwidth $B = (\omega_2 - \omega_1)/2\pi$ and Doppler cone angle interval $\vartheta_2 - \vartheta_1$. Transformation between (a) and (b) is called Stolt interpolation [4] for linear aperture SAR.

fundamental parameters which define the resolution are therefore aperture angle $\vartheta_2 - \vartheta_1$ and relative range bandwidth B/λ_c .

Many different algorithms have been devised for SAR image formation over the years (for a recent review, see [4]). The early work during the 1950s and 1960s concentrated on algorithms for the special case of a narrow bandwidth and aperture angle, leading to a quadratic phase expansion similar to the Fresnel approximation in optics. The rectangular format algorithm proved useful for implementation and fast Fourier transform (FFT) techniques could be used to provide computationally efficient algorithms. Early efforts to achieve fine resolution using large bandwidth and aperture angle were complicated by the motion of the object through many resolution cells in the pulse echo data. An approximate solution to this problem was provided by the polar format algorithm which appeared in the early 1970s [5]. Exact solutions, however, to the linear-aperture SAR problem appeared for the first time in the mid-1980s. These are known as the Fourier-Hankel [6–8] and range-migration (or ω -K) [9–11] inversion methods. Both are frequency-domain methods and may be implemented using fast transform algorithms, e.g. FFT and fast Abel transform, together with Stolt interpolation [4] in frequency domain. A major shortcoming of the algorithms, however, is that they are derived for a linear aperture and not easily extendible to the common nonlinear case. It is possible to partly correct for nonlinear motions, i.e. deviations from a linear track, but the image must be cut into small subimages and processed separately since the motion correction is only locally valid. The fast transform algorithms then become less efficient. This problem did not appear in past work with microwave SAR since the antennas used have a narrow beamwidth. However, it does become a major issue in wide-beam systems, e.g. low-frequency SAR where a wide beam is necessary to obtain acceptable resolution. Other major shortcomings of the frequency domain techniques are: 1) they require

a large computer memory to store and evaluate the two-dimensional frequency transforms, and 2) a significant amount of zero-padding in time domain is required before Stolt interpolation can be applied to data from a finite aperture without introducing cyclic convolution effects.

There is clearly a need for other processing algorithms which can be more easily adapted to a general aperture geometry. The most obvious solution to this problem is to implement the image formation in time domain. The latter can be considered a generalization of classical spatial beam-forming or matched filtering with a known signal embedded in Gaussian noise, i.e. for each image pixel the expected signal is used as a reference kernel in correlation processing. An equivalent way of considering such an algorithm is that of back-projection used in tomography [12]. It can be shown that the back-projection is equivalent to the Fourier-Hankel inversion for the linear-aperture SAR geometry [6, 8]. In the direct back-projection method, each received radar echo is processed and back-projected over spherical shells to all imaged ground pixels. Each pixel is thus assigned a value by interpolating the pulse echo at the time delay corresponding to the range between the pixel and the antenna. The values for each pixel are accumulated as more radar echoes are processed until all echoes have been processed and the final resolution achieved. Filtering of the data is also necessary to reconstruct the correct spectral weights of the data. The main drawback with the direct back-projection algorithm is the large number of operations required. The number of operations required for the direct back-projection algorithm is proportional to N^3 for an image with $N \times N$ pixels and N aperture positions, since every aperture position must be examined for every image pixel.

Recently, algorithms have been suggested which provide a speed-up of the filtered back-projection algorithm for SAR inversion. They operate in the time domain and include two-stage [13–15] and multiple-stage back-projection [16–18]. These algorithms exploit the fundamental redundancy between nearby aperture positions for high-frequency reflectivity components in the along-track direction. The number of operations required for the multi-stage algorithms are proportional to $N^2 \log_2(N)$, whereas the two-stage algorithms are proportional to $N^{2.5}$, i.e. both less than N^3 . Related fast algorithms have also appeared in the tomography community [19–23].

We propose the factorized back-projection (FBP) algorithm for SAR inversion based on recursive partitioning of the back-projection integral. Earlier work has been reported in [24–26]. It is shown to include the above-mentioned direct (single-stage) back-projection algorithm as well as two- and multiple-stage algorithms as special cases. It thus provides a unifying framework for different

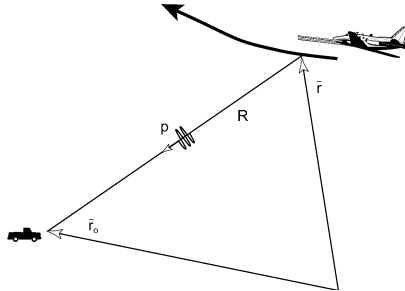


Fig. 2. Generic SAR imaging geometry. Pulse $p(R)$ propagates between antenna and object, and back again after being back-scattered by object.

back-projection algorithms. The work presented here is structured as follows. First the basic elements of the direct back-projection method is given and we discuss the reason for the heavy computational burden. The FBP algorithm is then introduced and analyzed concerning error propagation and computational burden. Finally, we propose and describe a practical and flexible algorithm implementation based on sequentially applying FBP on aperture blocks. Image examples are also included to illustrate algorithm performance.

II. RADAR ECHO MODEL

Consider a radar which transmits pulses from an antenna with little directivity and receives the back-scattered echo as a function of delay time. We restrict the present treatment to the mono-static case, i.e. we assume that the transmit and receive antennas are collocated. We assume a linear propagation medium which is isotropic, homogeneous, and nondispersive, i.e. the wave velocity c is constant in space. The ground is also assumed to be a collection of single-scattering objects (Born approximation) so that superposition applies. With these assumptions, the radar echo data can be modeled as illustrated in Fig. 2.

For a single point-like object at position \bar{r}_o the two-way response with the radar antenna positioned at \bar{r} is given by

$$g(\bar{r}, R) = \frac{p(R - |\bar{r} - \bar{r}_o|)}{|\bar{r} - \bar{r}_o|^2} \quad (2)$$

where $p(R)$ is the band-limited radar pulse after pulse compression, R (range) is the delay time t scaled by $c/2$, and it is assumed that the antenna and object are in the far-field of each other.

Although (2) is restricted to the case when the antenna and object are stationary relative to each other, we can often also use it for slowly moving platforms. This is called the “start-stop approximation” and is commonly used in SAR since the platform speed is much less than the speed of light. However, its validity needs to be evaluated in

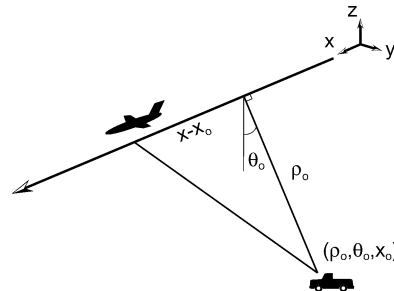


Fig. 3. Cylindrical coordinate (ρ, θ, x) system for representing ground reflectivity.

each particular imaging case. We assume here that the approximation is valid and refer the interested reader to [27].

Equation (2) neglects a number of scaling factors such as the responses of the antenna and object. These are in general complex functions of frequency, polarization, and direction. For simplicity, we assume that these factors can be set equal to 1. In practise, corrections for such effects are evaluated using stationary-phase methods [28].

The model in (2) is quite general and can be applied to most SAR problems. The simplest case is the linear-aperture SAR, i.e. a radar antenna moving along a linear track. In this case we have cylindrical symmetry around the track axis and (2) can be greatly simplified. We thus introduce cylinder coordinates (ρ, θ, x) with x being the along track axis as shown in Fig. 3. The range history for a single object now has a hyperbolic dependency on x , and the radar echo data are given by

$$g(x, R) = \frac{p \left(R - \sqrt{(x - x_o)^2 + \rho_o^2} \right)}{\left(\sqrt{(x - x_o)^2 + \rho_o^2} \right)^2}. \quad (3)$$

Note that the equation does not include the (elevation) angle coordinate θ_o of the object. This means that the cylindrical symmetry implies rotational invariance, i.e. the elevation angle is undetermined. The result is that objects from both sides of the aircraft will contribute to the same image pixel, i.e. corresponding to topographic as well as right-left ambiguities. The latter effect may be suppressed by antenna directivity in the elevation plane. On the other hand, the rotational symmetry means that a SAR image from a linear track can be formed without any knowledge of the ground topography which is a significant advantage.

III. SAR INVERSION USING BACK-PROJECTION

A. Back-Projection Integral

The exact inversion of the linear-aperture SAR problem can be solved using the Fourier-Hankel or filtered back-projection method [6, 8]. We use

(3) for the radar echo data as the starting point for deriving the filtered back-projection inversion. The fundamental principle is to generate a radar map of two cylindrical coordinates, i.e. a map where each object is located at its 2-parametric position (x, ρ) . The radar map is assumed to be a linear transformation from the radar echo data so that superposition of imaged point objects applies. We introduce the back-projected signal $h(x, \rho)$ according to

$$h(x, \rho) = \int_{-\infty}^{+\infty} g(x', R) R dx' \quad (4)$$

where $g(x, R)$ is the radar echo data as a function of along-track position x and range R , $R = \sqrt{(x' - x)^2 + \rho^2}$, and x' is the along-track integration parameter. For each image position (x, ρ) , the along-track integral sums the value from each radar echo at the range corresponding to the distance between the antenna and image position. In practise, the radar echo data is a discrete-time signal which has been sampled from the original continuous-time signal according to the Nyquist criteria. The bandwidth in the radial direction is determined by the pulse bandwidth, whereas the bandwidth in the along-track direction is determined by the maximum frequency (see Fig. 1(a) and (1)). It follows that the radar echo can be interpolated to arbitrarily accuracy using an appropriate interpolator kernel, e.g. a weighted sinc interpolator. Therefore, the integral (4) can be evaluated for an arbitrary image position by interpolating the discrete-time radar echo data.

We can also consider the integral (4) from the back-projection perspective, i.e. each interpolated radar echo is spread out over the imaged ground like a sun fan. The back-projected data will thus have constant values along concentric spheres, or circles in the 2-dimensional case, centered on the antenna phase center.

Evaluation of the Fourier transform of (4) is straightforward and results in

$$H(k_x, k_\rho) = 2\pi \int_{-\infty}^{+\infty} \int_0^{+\infty} g(x, R) R^2 J_o(R \sqrt{k_x^2 + k_\rho^2}) \times \exp(-jk_x x) dR dx. \quad (5)$$

Inserting the radar echo model (3) and assuming that the pulse has infinite bandwidth, i.e. the pulse is a Dirac delta-function $p(R) = \delta(R)$, results in

$$H(k_x, k_\rho) = 4\pi \exp(-jk_x x_o) \int_0^{+\infty} J_o(\sqrt{k_x^2 + k_\rho^2} \sqrt{x^2 + \rho_o^2}) \times \cos(k_x x) dx. \quad (6)$$

Equation (6) is a standard cosine transform which evaluates to

$$H(k_x, k_\rho) = 2\pi \frac{\exp[-j(k_x x_o + k_\rho \rho_o)] + \exp[-j(k_x x_o - k_\rho \rho_o)]}{|k_\rho|}. \quad (7)$$

After rearranging the ramp filter in the denominator to the left-hand side and inverse Fourier transformation we formally obtain the exact inversion result

$$\begin{aligned} F^{-1}\{|k_\rho| H(k_x, k_\rho)\} \\ = 2\pi[\delta^{(2)}(x - x_o, \rho - \rho_o) + \delta^{(2)}(x - x_o, \rho + \rho_o)] \end{aligned} \quad (8)$$

where $\delta^{(2)}(x, \rho) = \delta(x)\delta(\rho)$ is the two-dimensional Dirac-function. The back-projected and filtered radar echo data thus produce two Dirac-functions, one located at (x_o, ρ_o) and the other at $(x_o, -\rho_o)$. The latter is discarded since $\rho > 0$ by definition. Since superposition applies we may add an arbitrary number of point objects at different locations and with different amplitudes, and (8) will provide us the exact scene inversion.

In theory, the linear-aperture SAR problem can therefore be solved exactly and unambiguously by assuming that the Born approximation is valid. In practise, however, the ground is three-dimensional whereas the linear-aperture SAR is only capable of reconstructing the two-dimensional cylindrical projection of the scattering distribution, i.e. the ground represented in cylindrical coordinates with the two-dimensional distribution defined in terms of x and ρ . This means that the full three-dimensional ground cannot be retrieved without ambiguities. Given a topographic ground surface, ambiguities appear due to shadowing, layover as well as left/right-ambiguity. The latter are ambiguities arising from the ground on the opposite side of the linear track. Such ambiguities may be adequately reduced by introducing antenna directivity to suppress the unwanted ambiguous signals as mentioned earlier. The shadowing and layover ambiguities, however, are not possible to avoid but can be mitigated by using multiple flight tracks which provide different illumination geometry.

B. Extension to Nonlinear Track

The back-projection integral is easily modified to handle a general flight track geometry. A complication for nonlinear tracks is that data inversion becomes a 3-parameter problem which strictly speaking would require a two-dimensional aperture to solve exactly. However, in most cases only a one-dimensional aperture is available and the focusing becomes dependent on ground topography. The back-projection integral is therefore expressed as a function of the three-dimensional image position vector \bar{r}_o according to

$$h(\bar{r}_o) = \int g(x', R) R dx' \quad (9)$$

where $R = R(x') = |\bar{r}(x') - \bar{r}_o|$ is the range from the antenna to the image position, and the other parameters are defined as in (4). Equation (9) is able to handle any track geometry including, for example,

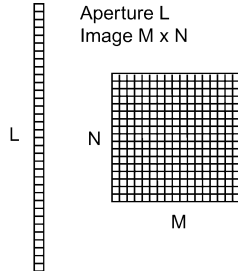


Fig. 4. Illustration of aperture (L) and image ($M \times N$) data used for SAR processing.

circular tracks as well as multiple repeat tracks. However, exact inversion is not guaranteed unless the track is linear.

C. Extension to Demodulated Signals

The formulation above has been restricted to the case when the radar echo is sampled including the carrier signal. This is a convenient and compact representation for ultrawideband signals but care must be taken when applying it to a bandpass signal. For narrowband signals, it is customary to demodulate the signal to baseband and use I and Q complex signal representation. For demodulated signals, we need to modify the back-projection integral (9) to include a multiplication with a phase factor according to

$$h(\bar{r}_o) = \int g(x', R) R \exp(j2k_c R) dx' \quad (10)$$

where k_c is the demodulation frequency.

D. Computational Burden

We have seen that the direct back-projection algorithm is robust and easy to understand, but in terms of number of operations it is very inefficient. Consider the case in Fig. 4, i.e. an image with $M \times N$ pixels and an aperture with L positions. For each aperture and pixel position we need to compute the range between the antenna and the pixel, interpolate the radar echo, and finally accumulate to the image matrix. When working with demodulated signals, we also need to perform a complex multiply to correct the phase. In total, the number of operations is therefore proportional to $L \times M \times N$. The latter is a very large number which limits the use of the algorithm to relatively small aperture and image sizes. For small images, direct back-projection is quite efficient and often preferred due to its simplicity and robustness. The algorithm has another major advantage in that it conserves memory requirements. Besides the image matrix, it is necessary to store only a single radar echo in memory. As soon as the radar echo has been back-projected to all image pixels it can be discarded.

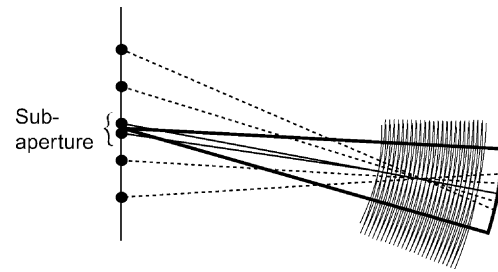


Fig. 5. Subaperture beam formation.

Each radar echo is then used in succession to form the back-projection integral.

IV. FACTORIZED BACK-PROJECTION

A. Back-Projection in Polar Coordinates

As mentioned above, the back-projection integral, (4) or (9), is very ineffective in terms of numerical performance. A careful analysis, however, reveals that, by a clever choice of coordinate system, it is unnecessary to back-project the aperture data to all image pixels for every new aperture position. This can be understood by considering the geometry in Fig. 5. The figure shows concentric range circles centered on different aperture positions, i.e. circles along which the range-compressed data are spread out over the subimage. Note that adjacent aperture positions have essentially the same circular pattern within the delineated “beam,” i.e. the triangular-shaped subimage. The circles shown have been matched along the beam center line, which corresponds to beam focusing in this direction. It also means that a single range line of data can be used to represent an angular sector with little error (see below for an error analysis). For points further away from the line, however, the circular patterns diverge corresponding to increasing phase errors. An effective way to represent the data in the image plane is therefore to use a polar coordinate system.

The number of data samples which are required to represent a subimage without loss of information increases with the length of the aperture data segment (subaperture). Alternatively, the subimage angular extent may be narrowed when the subaperture length increases in order to keep the number of data samples constant. This is the fundamental principle which enables computationally efficient back-projection algorithms to be constructed. As shown in the following, it is advantageous to split up the computations in a number of processing stages using polar coordinates instead of directly forming the Cartesian image with full resolution. In each processing step, finer angular resolution is obtained by combining coarse resolution beams along increasing subaperture lengths. In the last processing stage,

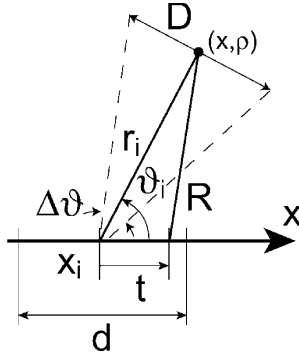


Fig. 6. Polar coordinate representation (r_i, ϑ_i) of back-projected data from subaperture d .

the image is formed in Cartesian coordinates with full spatial resolution. The class of SAR processing algorithms, which are based on this principle, we call FBP algorithms.

B. Subaperture Partitioning of Back-Projection Integral

The first step in deriving FBP is splitting up the back-projection integral (4) into an infinite sum over finite subapertures. We therefore define a back-projection integral over subaperture i of length d according to

$$h_d(x_i, r_i, \vartheta_i) = \int_{-d/2}^{d/2} g(x_i + t, R) R dt \quad (11)$$

with x_i is the along-track position of the subaperture center, (r_i, ϑ_i) are polar coordinates with origin centered on the subaperture as illustrated in Fig. 6, and $R = \sqrt{t^2 + r_i^2 - 2tr_i \cos \vartheta_i}$ is the range between the aperture and image points. The local polar coordinates are defined by $r_i = \sqrt{(x - x_i)^2 + \rho^2}$ and $\vartheta_i = \arctan[\rho/(x - x_i)]$ where (x, ρ) are the Cartesian coordinates of the image point.

By extending the integration limits in (11) to infinity we obtain (4) but in polar coordinate representation. The back-projection integral (4) may now be divided into an infinite sum over equal-length subapertures according to

$$h(x, \rho) = \sum_{i=-\infty}^{+\infty} h_d(x_i, r_i, \vartheta_i) \quad (12)$$

where index i is an integer $(..., -1, 0, 1, ...)$ corresponding to subaperture i . The center position of each subaperture is given by $x_i = x_0 + id$ where x_0 is the center position of subaperture $i = 0$.

By changing the subaperture length in (12) we may construct different but equivalent representations of the back-projection integral (4). This may be shown by partitioning the subaperture integral (11) into n

subapertures of shorter lengths according to

$$\begin{aligned} h_d(x_i, r_i, \vartheta_i) &= \sum_{j=-(n-1/2)}^{+n-1/2} h_{d/n}(x'_j, r'_j, \vartheta'_j) \\ x'_j &= x_i + j \frac{d}{n} \\ r'_j &= \sqrt{(r_i \cos \vartheta_i + x_i - x'_j)^2 + (r_i \sin \vartheta_i)^2} \\ \vartheta'_j &= \arctan[r_i \sin \vartheta_i / (r_i \cos \vartheta_i + x_i - x'_j)] \end{aligned} \quad (13)$$

where j is an integer when n is odd, or an integer $+ \frac{1}{2}$ when n is even. By inserting (13) into (12) we obtain an equivalent representation in terms of the shorter subaperture integrals according to

$$\begin{aligned} h(x, \rho) &= \sum_{i=-\infty}^{+\infty} h_d(x_i, r_i, \vartheta_i) = \sum_{i=-\infty}^{+\infty} \sum_{j=-\frac{n-1}{2}}^{+\frac{n-1}{2}} \\ &\times h_{d/n}\left(x_0 + (ni + j)\frac{d}{n}, r'_j, \vartheta'_j\right) \\ &= \sum_{l=-\infty}^{+\infty} h_{d/n}\left(x_0 + l\frac{d}{n}, r'_l, \vartheta'_l\right) \end{aligned} \quad (14)$$

where l is an integer when n is odd, or an integer $+ \frac{1}{2}$ when n is even.

The back-projection integral (4) may thus be determined recursively by partitioning longer subapertures into a sum over shorter subapertures until the original pulse echo data is obtained. Conversely, the back-projection integral may be computed, without approximations, by summation of successively longer subaperture starting from the original pulse echo data.

The FBP algorithm is a discrete version of recursively applying (14), i.e. the continuous functions are approximated by sampled functions at a finite number of discrete points which are chosen to minimize the sampling error. In the following sections, we analyze the resulting algorithm error. When analysing SAR processing algorithms, it is common practise to consider phase errors. However, we also discuss range errors which are useful in ultrawideband SAR processing. The phase error can be obtained by multiplying the range error by $2k$ where k is the wavenumber.

C. Sampling Requirements

The FBP algorithm relies on splitting the back-projection integral according to (12) and (14) where data in each subaperture is represented in local polar coordinates. The angular bandwidth of the data increases for increasing subaperture length in the same manner as for beam formation from an aperture. This means that the number of beam positions which are required for Nyquist sampling of

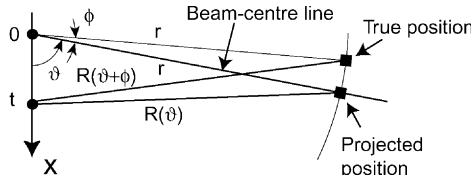


Fig. 7. Range error introduced by nearest neighbor interpolation in angle.

the data increases with subaperture length. When the range is much larger than the aperture, i.e. $|t/r| \ll 1$, the range can be approximated by $R = r - t \cos \vartheta$. Using stationary-phase evaluation of the Fourier transform it can be shown that the following sampling requirements apply [15]

$$\Delta r \leq \frac{c}{2B} \quad (15)$$

$$\Delta(\cos \vartheta) \leq \frac{\lambda_{\min}}{2d}. \quad (16)$$

The factor 2 in the denominators are due to the two-way propagation delay in mono-static radar.

A general expression for the sampling requirements, i.e. which is valid for all aperture sizes, is difficult to derive in closed form. It is clear that the same requirement (15) applies to the radial coordinate, whereas the angular sampling requirement will have a different form from (16). Instead of attempting to derive the latter, however, we derive a general expression for the worst case range error across the beam which essentially provides the same result.

D. Range Error Analysis

In this section, we consider the range error introduced by representing the back-projected data within an angular sector by a single subaperture range line. This corresponds to the case of nearest neighbor interpolation in angle, but other interpolation schemes may be analyzed with the same method. Data in the range direction, on the other hand, are for simplicity assumed to be interpolated with negligible error. This is a reasonable assumption since range interpolation is effectively performed with little extra cost using FFT and zero-padding in combination with a low-order interpolator. The geometry is illustrated in Fig. 7 which shows a beam-center range line at angle ϑ , where back-projected data are accumulated during a subaperture according to (11). Note that along this line the back-projection is performed without geometrical errors in angle. However, a range error is introduced when assigning back-projected data outside the beam-center line. The value at the “true position” $(r, \vartheta + \phi)$ in Fig. 7 is approximated by the value at the “projected position” (r, ϑ) .

The cosine theorem gives the range R from any image position to a point along the aperture t (relative

to the subaperture mid-point) according to

$$R(\vartheta)^2 = r^2 + t^2 - 2rt \cos \vartheta \quad (17)$$

and the range error is therefore expressed by

$$\begin{aligned} \Delta R &= R(\vartheta + \phi) - R(\vartheta) = \sqrt{r^2 + t^2 - 2rt \cos(\vartheta + \phi)} \\ &\quad - \sqrt{r^2 + t^2 - 2rt \cos(\vartheta)}. \end{aligned} \quad (18)$$

We can evaluate the range error using the approximation

$$\Delta R \approx \frac{R(\vartheta + \phi)^2 - R(\vartheta)^2}{2R(\vartheta)} \quad (19)$$

which assumes that the range error is much smaller than the range, i.e. $|\Delta R| \ll R$. Combining (18) and (19) leads to the range error expression

$$\Delta R \approx rf(t/r, \vartheta)[\cos(\vartheta) - \cos(\vartheta + \phi)] \quad (20)$$

where we have separated the dependency of ϕ and t in different factors and the function f is defined by

$$f(s, \vartheta) = \frac{s}{\sqrt{1 - 2s \cos(\vartheta) + s^2}}. \quad (21)$$

A plot of (21) for different values of ϑ is shown in Fig. 8. It can be shown that the range error is bounded by

$$|\Delta R| \leq \frac{\min(|t|, r)}{\sin \vartheta} |\cos(\vartheta) - \cos(\vartheta + \phi)|. \quad (22)$$

Note that the error bound increases linearly with $|t|$ up to $|t| = r$ after which it becomes constant as indicated in Fig. 8. This corresponds to the approximately linear increase in Doppler bandwidth as the synthetic aperture increases as long as the aperture angle is small (far-field approximation).

The worst case error over a symmetric aperture of length d is therefore bounded by

$$|\Delta R| \leq \frac{\min(d/2, r)}{\sin \vartheta} |\cos \vartheta - \cos(\vartheta + \phi)|. \quad (23)$$

Equations (18), (20), and (22) are general expressions for the range error with different approximations. A further simplification can be obtained when the angle fulfills the condition $\phi \ll \min(1, \tan \vartheta)$. The resulting small-angle error bound within a beam of full width $\Delta\vartheta$ is thus given by

$$|\Delta R| \leq \begin{cases} \frac{d\Delta\vartheta}{4} = \frac{dD}{4r}, & d \leq 2r \\ \frac{r\Delta\vartheta}{2} = \frac{D}{2}, & d > 2r \end{cases} \quad (24)$$

where D is the subimage width as shown in Fig. 6. Equation (24) is quite useful for a side-looking SAR, whereas forward- or backward-looking systems may require using the more accurate forms above. From (24), it is clear that we can balance an increase in subaperture d by decreasing the subimage D in order to keep their product and hence the range error constant. However, when the subaperture d becomes

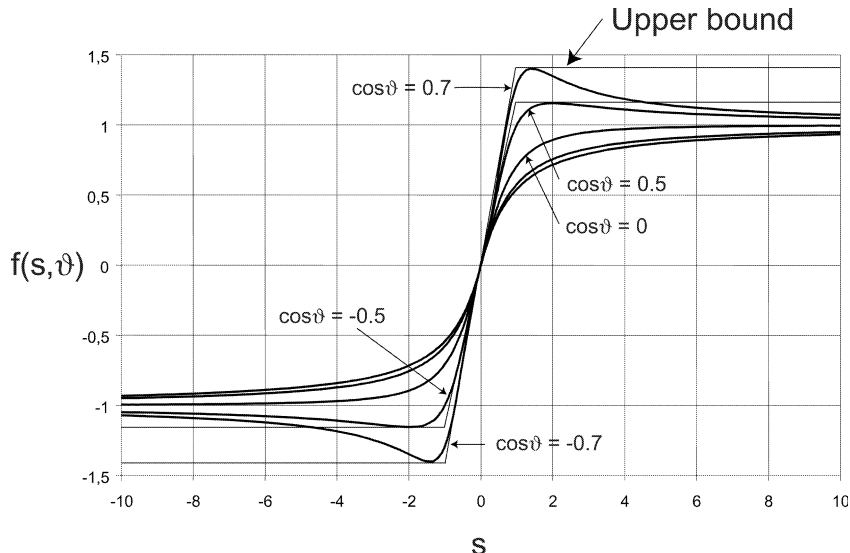


Fig. 8. Function $f(s, \vartheta)$ illustrated for $\cos \vartheta = 0, \pm 0.5, \pm 0.7$.

larger than $2r$ there is no longer a need to decrease the subimage size according to (24). The reason is that the resolution then increases very slowly since Doppler cone angle changes very slowly.

We can also derive a small-angle error bound directly from (20) by assuming $d \ll r$ which gives a slightly tighter upper bound compared with (24)

$$\Delta R \approx d \sin \vartheta \Delta \vartheta = d \Delta(\cos \vartheta) \quad d \ll r. \quad (25)$$

The sampling requirement (16) follows directly from (25) by setting $2k_{\max} |\Delta R| = \pi$, i.e. $|\Delta R| = \lambda_{\min}/4$. Similar sampling requirements may thus be derived from the more general range error expressions above.

The equations derived for the maximum range error, (23)–(25), are valid for each subaperture whereas the total error in the resulting SAR image requires accumulation in all subapertures processing stages. An estimate of the total error is therefore necessary in order to characterize the performance of the FBP algorithm. We estimate the error by considering the distortion for a single point object in position (x_o, ρ_o) , i.e. the loss in maximum amplitude caused by the FBP algorithm. Any range error introduced by the algorithm will reduce the maximum amplitude and consequently increase sidelobe energy. Let $q(x, \rho)$ be the ideal point object response and $q_{\text{FBP}}(x, \rho)$ the response using the FBP algorithm. The relative error after accumulation in each stage is thus approximately given by

$$\frac{|q_{\text{FBP}}(x_o, \rho_o) - q(x_o, \rho_o)|}{|q(x_o, \rho_o)|} \approx 2k \langle \Delta R \rangle \quad (26)$$

provided the individual phase errors $2k \Delta R$ are small and where $\langle \Delta R \rangle$ is the range error averaged over all subapertures and stages. We note that the positive and negative range errors in Fig. 8 over a subaperture tend to cancel each other. This suggests that the maximum

range errors are, in fact, conservative estimates of the total error. It should also be noted that the point object response is not shift-invariant using the FBP algorithm. It varies slightly over the image depending on the exact spatial location of the various subaperture beams used to form a particular image pixel value.

Equations (11)–(13) and (24) are the basis for designing the FBP algorithm. By summation along a subaperture, the aperture data are transformed from (x, R) coordinates without angular resolution to polar coordinates (r, ϑ) with angular resolution proportional to subaperture length. A new set of aperture data are thus generated with improved angular resolution and essentially without loss of information content. At the same time, the aperture sampling rate given by the reciprocal of the distance between subaperture centers is proportionally reduced so that the total number of independent points in the data matrix is constant. Each new data point is computed by interpolating and summing a small number of aperture points at the corresponding range and angle.

The main design parameter of the FBP algorithm is the maximum range error which can be accepted for adequate image quality. The latter depends on the application in question as well as the competing noise sources. Hence it should be tuneable in the algorithm implementation.

E. Aperture Factorization

We now describe the factorization of the aperture and estimate the resulting computational burden. Consider again the problem shown in Fig. 4, i.e. an aperture L and an image $M \times N$. Suppose we are able to find a factorization of L into K integer factors corresponding to K processing stages according to

$$L = l_1 \times l_2 \times \cdots \times l_K. \quad (27)$$

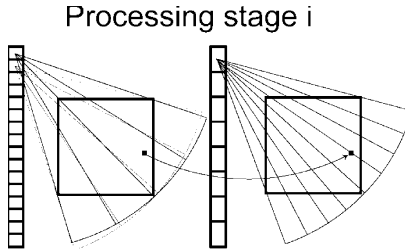


Fig. 9. FBP algorithm performs subaperture summation and beam formation in each processing stage. In this example, the number of subapertures are reduced by a factor 2 and the number of beams are increased by a factor 2. “New” beam position is indicated by a black square, at which back-projected data is computed by interpolation in range and angle of data from two “old” sets of beams corresponding to two subapertures.

Each factor l_i ($i = 1, \dots, K$) defines the reduction in the number of aperture positions l_i during processing stage i . One or more beams are associated with each aperture position, i.e. the beams represent radar data in local polar coordinates centered on the aperture position. In each stage, a number of new beams are formed by summation of beams from the previous stage using range and angular interpolation as illustrated in Fig. 9. The number of range and beam positions required for each stage is defined by the image quality requirements as well as the method used for interpolation. The described principle relies on using (24) to equalize the phase error among processing steps. Hence, the subaperture lengths and beam spacing are inversely related to keep their product constant.

Suppose, for simplicity, equal image and aperture dimensions ($L = M = N$) as well as a common factorization throughout all stages ($l_i \equiv n$ for all i), that is $L = n^K$. We also assume that the range and aperture sample spacings are equal.

In the first processing stage, we create beams which span the image from the new subaperture centers along track. Each new subaperture center has associated n new beams generated from n original aperture positions. This means that the original aperture has been split into L/n subapertures, each of length n . The number of operations to form the beams is therefore proportional to (subapertures) \times (subaperture points) \times (beams) \times (beam samples), i.e. $(L/n) \times n \times n \times M = nM^2$ since L is assumed equal to M .

In the second processing stage we again form new beams but this time based on the beams formed in the previous stage. Each new subaperture center now has associated n^2 new beams, and the number of subapertures is L/n^2 . The number of old subaperture centers which are used to form a new beam is n , i.e. the number of operations is therefore proportional to $(L/n^2) \times n \times n^2 \times M = nM^2$. The number of operations in the second stage, as well as in the following stages, is therefore the same as in the first processing stage.

The algorithm continues in a similar manner until the last stage where the computed beam points are located on a Cartesian grid. The final image with full resolution is thus obtained and all original aperture positions have been combined into a single long aperture. Each processing stage has the same number of operations so that the total number to form an image is given by

$$OP \propto nM^2K = nM^2 \log_n M. \quad (28)$$

The minimum operations count of (28) is obtained for $n = e$. In practise, n is required to be an integer which leads to a broad minimum around $n = 3$. It is interesting to note that $n = 2$ and $n = 4$ gives the same number of operations and only 6% more than the minimum value. The savings in number of operations compared with the direct back-projection algorithm is given by

$$\frac{(OP)_{\text{bp}}}{(OP)_{\text{fbp}}} \propto \frac{M}{n \log_n M}. \quad (29)$$

The computational savings is thus large whenever the aperture and image is large. Using $n = 2$ or 4, the ratio according to (29) is 170 for $M = 4096$ and 590 for $M = 16384$. This is a significant reduction in computational effort and corresponds to the improvement obtained by the FFT algorithm compared to the direct implementation of the discrete Fourier transform (DFT). Hence, the FBP algorithm has a computational effort of the same order of magnitude as the Fourier Hankel and range migration algorithm.

The final image quality is mainly controlled by the performance of the angular interpolation method used. The reason for this fact is that the oversampling ratio, i.e. angular sampling rate divided by the Nyquist rate, is constant through the processing stages since an increase in subaperture length is exactly balanced with a reduction in beam spacing. Using nearest neighbor interpolation in angle, the maximum range error in each processing stage using (24) is given by

$$|\Delta R| \leq \frac{N\delta_N\delta_L}{4R_{\min}} \quad (30)$$

where δ_N and δ_L is the image pixel and aperture spacing, respectively, R_{\min} is the closest range to the image and $N\delta_N$ is the image extent in the along-track direction. The maximum range error is, in this case, defined by the maximum angular extent of the image as seen from the aperture and the aperture spacing. A typical requirement is to keep the phase error below $\pi/8$ at the center frequency, which, in the example, corresponds to a maximum image size of $N_{\max} = \lambda_c R_{\min} / 8\delta_N\delta_L$.

This described method may be improved to process arbitrary image sizes independent of the minimum range. The basic algorithm is therefore modified by defining the beam spacing in the first

stage to control the range error according to (24). This method avoids restricting the maximum image size (or minimum range) by instead increasing the number of beams. In the subsequent processing stages, the same principle as described above is used, i.e. an increase in subaperture length l_i is exactly balanced by a reduction in beam spacing according to (24).

F. Block-Factorized Back-Projection Algorithm

We now describe one FBP algorithm implementation which has proven to be flexible and provide good numerical performance. In principle, we may have arbitrary aperture, image size, and minimum range provided the factorization constraints are fulfilled. Nearest neighbor interpolation is used in angle, whereas zero-padding in frequency domain followed by inverse FFT and a low-order interpolation is used in range. We require factorization of both the aperture and image sizes, i.e. besides (27) for the aperture we also use factorizations of the image sizes according to

$$M = m_1 \times m_2 \times \cdots \times m_K \quad (31)$$

$$N = n_1 \times n_2 \times \cdots \times n_K \quad (32)$$

where M and N correspond to the image range and azimuth directions, respectively. Each triplet (l_i, m_i, n_i) defines the increase in image pixels $m_i \times n_i$ and reduction in aperture positions l_i during processing stage i . All triplets should be chosen according to (24) in order to control the range error. The subimages resulting from the factorization define the beam spacing since each subimage has one crossing beam in this implementation. Besides limiting the beam spacing, image factorization in range has an additional purpose, i.e. it reduces the number of operations related to range computations. For each subaperture position, the range as well as the differential range are computed only to the center position for each subimage. The range to other beam positions are obtained by linear extrapolation using range and differential range. This method provides a significant savings in computational time since each range computation involves taking the square root and is thus numerically very costly.

A short-coming of the algorithm described in the previous section is the large amount of memory required to store the intermediate results. The problem is similar to the FFT algorithm which also requires a large memory. In fact, the amount of data in each stage of the algorithm is approximately the same for all stages which means that approximately twice the size of the raw data matrix is required. The block-FBP algorithm therefore divides the original aperture into a number of aperture blocks and applies the FBP algorithm to each. Data for each aperture block are successively read into memory, processed to the final

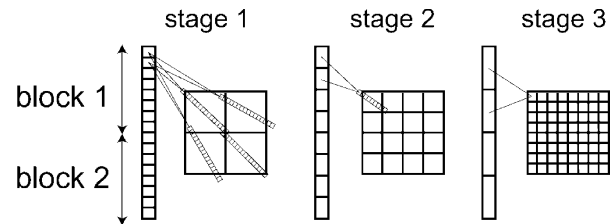


Fig. 10. Schematic illustration of block-FBP algorithm with $L = M = N = 8$ and $K = 3$ processing stages. All processing stages use a common factorization $n = 2$ in this example. First two processing stages use polar coordinates to represent back-projected data and form beams along radial direction from subaperture center point. Narrower “new” beams are formed based on wider “old” beams formed in previous stage. Last and third processing stage performs beam formation to image points in final rectangular Cartesian grid. Full aperture data is also split into two blocks which are read into memory and processed independently of each other until data are accumulated in stage 3. This procedure conserves memory when the two blocks are processed in succession since only one block of aperture data, final image grid, and intermediate results require memory storage.

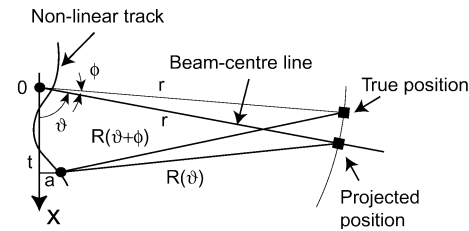


Fig. 11. Range error introduced by nearest neighbor interpolation in angle for nonlinear flight track.

image grid, and the output results from all blocks are accumulated. This procedure significantly conserves memory with a small penalty in computational effort. As an illustrative example, consider the factorization in Fig. 10 using 3 processing stages. The algorithm has constant factorization within a block of data and the full image grid is obtained when the aperture block is completed.

A quantitative example illustrates the memory savings. Consider a $4k \times 4k$ image which is formed from a $16k \times 8k$ aperture data matrix. Storing the image alone requires 128 Mbytes using complex floating point numbers whereas the aperture data require 1 Gbyte of memory plus intermediate results. By using an aperture block size of $1k$ the aperture data requirement reduces to $1k \times 8k$, i.e. 64 Mbytes, which is a significant savings.

G. Nonlinear Flight Geometry

The proposed FBP algorithm can handle nonlinear flight tracks without essential modifications. Motion deviations from a linear track is corrected for each back-projected data line by computing the range using the center coordinates for each subaperture and subimage including ground topography. A

new center position is assigned to each subaperture after completing the summation. Finer motion compensation is thus included by the algorithm as the resolution successively improves through the processing stages.

The effect of nonlinear motion may be analyzed in a similar way as the linear aperture, i.e. by determining the range error for a given subaperture size as a function of beam off-center angle ϕ as illustrated in Fig. 11. The assumption is again that nearest neighbor angular interpolation is used. The range error can be shown to be given by

$$|\Delta R| \leq \sqrt{d^2 + 4a^2} \frac{\Delta\vartheta}{4} = \sqrt{d^2 + 4a^2} \frac{D}{4r}, \quad d \leq 2r \quad (33)$$

where a is the across-track deviation from the linear track. The expression for $d > 2r$ is the same as in (24). The essence of (33) is that an across-track curvature may be mitigated by a slight reduction of either the subaperture or subimage size. Note also that larger across-track deviations may be tolerated for longer subapertures d . This is important since the across-track error typically is small for short track segments and increases with for longer segments. A nominally linear track therefore does not normally need any change in algorithm parameters, i.e. the successively larger across-track deviations when the subaperture size increases does not increase the resulting range error.

H. Comparison with Other Algorithms

The processing method discussed here has similarities with two recently proposed back-projection algorithms for SAR inversion. In fact, both may be considered as special cases of FBP. Local back-projection [13–15] is a special case of FBP using only two processing stages ($K = 2$). The first stage comprises subaperture beam formation using local polar coordinates, and the second stage performs back-projection to the Cartesian image grid. The optimum number of aperture points summed in each stage is equal to \sqrt{M} which gives a nominal complexity reduction compared with direct back-projection of $\sqrt{M}/2$ according to (29). The quad-tree algorithm [16] is based on subaperture beam formation in multiple processing stages with a factorization of 2 in each processing stage. It is thus a special case of the block-FBP algorithm with $l_i = m_i = n_i = 2$ and a single aperture block. Note, however, that the quad-tree algorithm retains only the zero-frequency component in each subimage whereas the FBP algorithm may use angular interpolation based on higher order components with improved accuracy. The quad-tree algorithm also needs to be complemented with a mechanism of controlling the algorithmic error which may otherwise lead to poor

image quality. The fast back-projection algorithm described in [17–18] is rather different but also related to FBP. It performs subaperture summation but splits the image into subimages of a different shape. The smaller and smaller subimages are regions defined by the intersections between circular arcs. Similar to the quad-tree algorithm it uses a factorization of 2 in each processing stage and a single aperture block. The theoretical numerical complexity is similar to FBP but this level of performance has not yet been obtained in practice.

V. EXAMPLE IMAGERY

The improved computational performance of factorized versus direct back-projection is significant. However, it is essential that image quality is not sacrificed despite the approximations introduced. On the other hand, there is no need to overdesign the processor in terms of image quality since other noise sources may dominate.

Image quality is a qualitative term which is difficult to define in a strict way. Clearly, the impulse response is essential and can be characterized by resolution, peak sidelobe ratio, and integrated sidelobe ratio, etc. Other characteristics like geometrical, radiometric and phase accuracy are also important for many applications.

We restrict the analysis here to processing the same radar data through the two processors and compare the resulting images. The choice of scene is clearly important since required image quality parameters are very scene dependent. We therefore deliberately choose a difficult scene which includes large scene contrasts and where the system noise is relatively low.

The comparison, shown in Figs. 12 and 13, is performed using images over the western parts of the city of Linköping, Sweden. Radar data were acquired with the airborne ultrawideband CARABAS SAR [13] operating in the 20–90 MHz frequency band which has an azimuth beamwidth of about 90°. The flight altitude was about 3 km and the track was measured using phase-differential GPS. The processing uses the GPS data as well as the average altitude above ground for motion corrections. Figs. 12 and 13 show the results from using direct back-projection and block-FBP, respectively. The results indicate that the two images are very similar in image quality but with a slightly (not visible) higher noise floor in the near-range for the factorized algorithm. The latter is caused by strong echoes from buildings in a suburban area in combination with the reduced ISLR (integrated sidelobe ratio, i.e. integrated mainlobe energy divided by integrated sidelobe energy).

The block-FBP algorithm was set up with an unequal factorization corresponding to a maximum range error of 0.12 m or 0.28 radians in each stage



Fig. 12. Scene over city of Linköping processed with direct back-projection algorithm. Aperture is 16384 samples at 0.94 m spacing, and image is 6400×8192 pixels at $1 \text{ m} \times 1 \text{ m}$ spacing. Slant range to near range of image is 4895 m and average altitude is 2811 m.

at the center frequency. The aperture block size was chosen to 256, i.e. the 16384 aperture positions in the raw data were divided into 64 blocks. Four aperture positions are summed in each processing stage until the entire block is processed which requires four stages. The fifth processing stage corresponds to summation over the 64 blocks. All processing stages thus correspond to an aperture factorization

according to $16384 = 4^4 \times 64$. Range factorization, which controls the range computation, is chosen to four according to $8192 = 4^4 \times 32$, i.e. a factor 4 in the first four stages and 32 in the final stage. Angular factorization is chosen to $6400 = 10 \times 4^3 \times 10$, i.e. a factor 10 in the first stage to reduce the range error, a factor 4 in the three following stages and a factor 10 in the final stage. Nearest neighbor interpolation



Fig. 13. Same as Fig. 12 but processed with block-FBP algorithm using 64 aperture blocks with 256 aperture positions in each blocks.

is performed in angle, and a quadratic interpolator is used in range.

An estimate of FBP computational efficiency compared with direct back-projection is given by $(16384 \times 8192 \times 6400)/(64 \times 8192 \times (2560 + 2560 + 2560 + 2560 + 6400)) = 98$. The value 2560 is the number of summations required to form the beams within the aperture block during each of the four first stages. In the first processing stage, for example, 4

aperture positions are used to form 10 beams for each of 64 subapertures. In the final stage, the full resolution image of size 6400×8192 is formed.

A comparison between the execution time for two algorithms resulted in a savings of about 300, i.e. 45 min instead of 9 days on a single-processor work station. This is a factor 3 more compared with the theoretically estimated 98. The reason that the FBP algorithm is even better than the estimate above is

Backprojection Algorithm

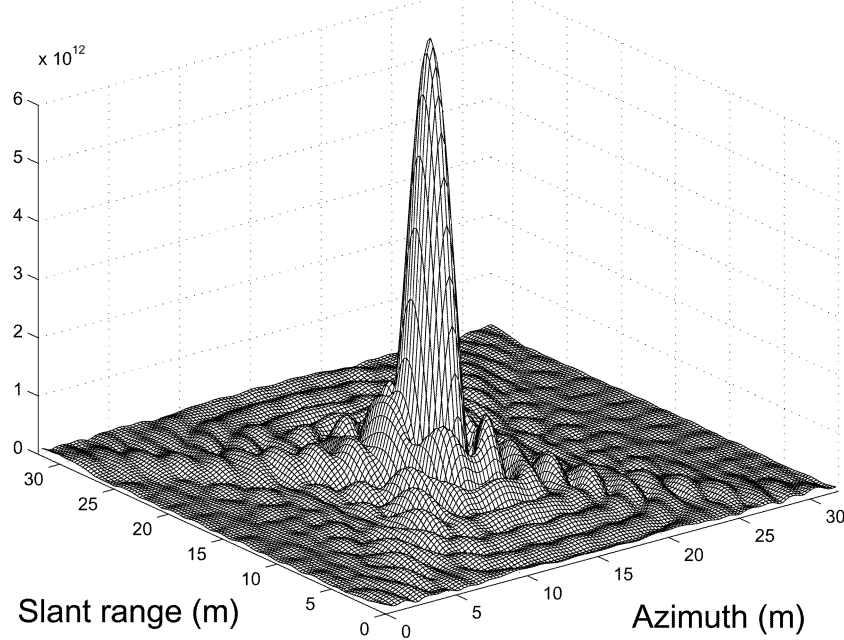


Fig. 14. Simulated impulse response function using direct back-projection algorithm. Raw radar data generated along linear aperture with 6000 samples at 0.83 m spacing. Ideal point target located at slant range of 2500 m and in middle of aperture. Result shows magnitude of complex impulse response.

Fast Backprojection Algorithm

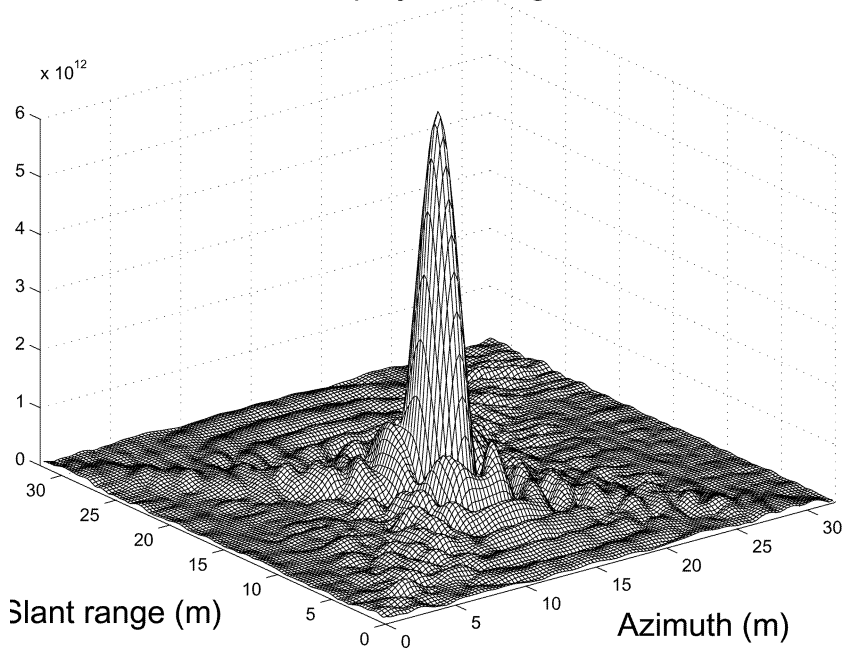


Fig. 15. Simulated impulse response function using block-FBP algorithm. Same raw radar data as in Fig. 14 was used. Worst case shown resulted in peak amplitude loss of slightly less than 1 dB.

due to the more effective range computation. In the direct back-projection, one range value is computed for each image pixel which includes an ineffective square root operation. In the FBP algorithm, only two range values using the square root are computed close to the center of each subimage whereas the other ranges are computed using linear extrapolation. This

provides a significant speed-up compared with the direct back-projection method.

Figs. 14 and 15 show another performance comparison between direct back-projection and block-FBP. Raw radar data was simulated along a linear aperture with 6000 samples at 0.83 m spacing. An ideal point target was located at slant range

2500 m and centered along the aperture. Fig. 14 shows the result of generating an image using direct back-projection. Note that the resulting impulse response is nonseparable in slant range and azimuth, and the curved nature of the range sidelobes. Note also the sidelobe arms which extend diagonally from the image center. They are a result of the finite-length aperture and may be reduced by proper spectral weighting. Fig. 15 shows a similar result by using block-FBP processing from the same raw data and with a maximum range error set to 0.13 m in each stage. The block-FBP impulse response varies slightly across the image due to changing range error. Fig. 15 shows the worst case when the peak amplitude loss is 1 dB compared with the direct back-projection. The amplitude loss may be reduced by decreasing the maximum range error.

VI. CONCLUSIONS

We have described and analyzed a general class of SAR processing algorithms which are based on recursive partitioning of the time-domain back-projection integral. The resulting factorized back-projection (FBP) algorithm consists of a number of processing stages and is suitable for ultrawideband SAR image formation since it is capable of handling large deviations from a linear flight track. Several earlier proposed fast back-projection algorithms may be considered as special cases. FBP provides the accuracy and robustness of a time-domain algorithm but with a computational performance in parity with fast transform algorithms, e.g. the Fourier-Hankel or range migration algorithms. Furthermore, it significantly conserves memory compared with frequency-domain algorithms. Algorithm factorization is based on equalizing the range (phase) error throughout the processing stages. Each processing stage forms a set of back-projected beams on the ground in local polar coordinates by summation of subapertures under the constraint of a constant range error. The subaperture length increases successively whereas the beamwidth decreases. Image quality is controllable by tuning the maximum range error. A practical implementation called block-FBP is also described which easily can trade-off image quality, operations count and memory size. The algorithm provides a significant reduction in computational burden of two to three orders of magnitude compared with direct back-projection for the considered airborne ultra-wideband SAR processing geometry.

REFERENCES

- [1] Cutrona, L. J., Vivian, W. E., Leith, E. N., and Hall, G. O. (1961) A high-resolution radar combat-surveillance system. *IRE Transactions on Military Electronics*, **5**, 2 (1961), 127–131.
- [2] Elachi, C. (1988) *Spaceborne Radar Remote Sensing: Applications and Techniques*. New York: IEEE Press, 1988.
- [3] Ulander, L. M. H., and Hellsten, H. (1996) A new formula for synthetic aperture radar resolution. *AEÜ, International Journal of Electronics and Communications*, **50**, 2 (1996), 117–121.
- [4] Carrara, W. G., Goodman, R. S., and Majewski, R. M. (1995) *Spotlight Synthetic Aperture Radar, Signal Processing Algorithms*, Boston: Artech House, 1995.
- [5] Walker, J. L. (1980) Range-Doppler imaging of rotating objects. *IEEE Transactions on Aerospace and Electronic Systems*, **AES-16**, 1 (1980), 23–52.
- [6] Fawcett, J. A. (1985) Inversion of N-dimensional spherical means. *SIAM Journal of Applied Mathematics*, **45** (1985), 336–341.
- [7] Hellsten H., and Andersson, L.-E. (1987) An inverse method for the processing of synthetic aperture radar data. *Inverse Problems*, **3** (1987), 111–124.
- [8] Andersson, L.-E. (1988) On the determination of a function from spherical averages. *SIAM Journal of Mathematical Analysis*, **19**, 1 (1988), 214–232.
- [9] Rocca, F., Cafforio, C., and Prati, C. (1989) Synthetic aperture radar: A new application for wave equation techniques. *Geophysical Prospecting*, **37** (1989), 809–830.
- [10] Cafforio, C., Prati, C., and Rocca, F. (1991) SAR data focusing using seismic migration techniques. *IEEE Transactions on Aerospace and Electronic Systems*, **27**, 2 (1991), 194–206.
- [11] Milman, A. S. (1993) SAR imaging by ω -k migration. *International Journal of Remote Sensing*, **14**, 10 (1993), 1965–1979.
- [12] Natterer, F. (1986) *The Mathematics of Computerised Tomography*, New York: Wiley, 1986.
- [13] Hellsten, H., Ulander, L. M. H., Gustavsson, A., and Larsson, B. (1996) Development of VHF CARABAS II SAR. In *Proceedings of Radar Sensor Technology*, SPIE AeroSense Conference, Orlando, FL, April 8–9, 1996; also *SPIE*, **2747** (1996), 48–60.
- [14] Seger, O., Herberthson, M., and Hellsten, H. (1998) Real-time SAR processing of low frequency ultra wide band radar data. In *Proceedings of EUSAR'1998*, Friedrichshafen, Germany, May 25–27, 1998, 489–492.
- [15] Yegulalp, A. F. (1999) Fast backprojection algorithm for synthetic aperture radar. In *Proceedings 1999 IEEE Radar Conference*, Waltham, MA, April 20–22, 1999, 60–65.
- [16] McCorkle, J., and Rofheart, M. (1996) An order $N^2 \log(N)$ backprojector algorithm for focusing wide-angle wide-bandwidth arbitrary-motion synthetic aperture radar. In *SPIE AeroSense Conference*, Orlando, FL, April 8–9, 1996; also *SPIE*, **2747** (1996), 25–36.
- [17] Nilsson, S. (1996) Fast backprojection. Report LiTH-ISY-R-1865, ISSN 1400-3902, Linköping University, Sweden, 1996.

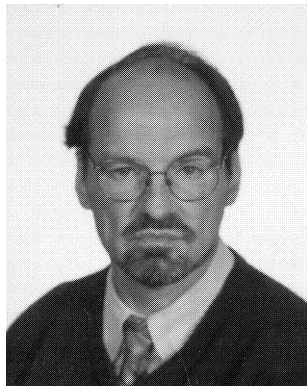
- [18] Nilsson, S. (1997)
Application of fast backprojection techniques for some inverse problems in integral geometry.
Ph.D. dissertation 499, Linköping University, Sweden, 1997.
- [19] Götz, W. A. (1993)
Eine schnelle diskrete radon transformation basierend auf rekursiv definierten digitalen geraden.
Ph.D. dissertation, University of Innsbruck, 1993.
- [20] Brady, M. L. (1998)
A fast discrete approximation algorithm for the radon transform.
SIAM Journal of Computing, **27**, 1 (1998), 107–119.
- [21] Brandt, A., Mann, J., Brodski, M., and Galun, M. (1999)
A fast and accurate multilevel inversion of the radon transform.
SIAM Journal of Mathematical Analysis, **60**, 2 (1999), 437–462.
- [22] Basu, S., and Bresler, Y. (2000)
 $O(N^2 \log_2 N)$ filtered backprojection reconstruction algorithm for tomography.
IEEE Transactions on Image Processing, **9**, 10 (2000), 1760–1773.
- [23] Basu, S., and Bresler, Y. (2001)
Error analysis and performance optimization of fast hierarchical backprojection algorithms.
IEEE Transactions on Image Processing, **10**, 7 (2001), 1103–1117.
- [24] Ulander, L. M. H., and Hellsten, H. (1999)
Low-frequency ultra-wideband array-antenna SAR for stationary and moving target imaging.
In *Proceedings of SPIE's 13th Annual International Symposium on Aerosense*, Orlando, FL, April 5–9, 1999; also *SPIE*, **3704** (1999), 149–158.
- [25] Hellsten, H., and Ulander, L. M. H. (2000)
Airborne array aperture UWB UHF radar motivation and system considerations.
In *Proceedings of the 1999 IEEE Radar Conference*, Waltham, MA, April 20–22, 1999, 47–53; also in *IEEE AES Systems Magazine*, (May 2000), 35–45.
- [26] Ulander, L. M. H., Hellsten, H., and Stenström, G. (2000)
Synthetic-aperture radar processing using fast factorised backprojection.
In *Proceedings of EUSAR'2000*, Munich, Germany, May 23–25, 2000, 753–756.
- [27] Hellsten, H. (1984)
Extraction of structural information from radar signals.
FOA report C 30370-E1, Swedish Defence Research Establishment, PO Box 1165, SE-581 11 Linköping, Sweden, ISSN 0347-3708, 1984.
- [28] Ulander, L. M. H., Frölind, P. O., and Martin, T. (1999)
Processing and calibration of ultra-wideband SAR data from CARABAS-II.
In *Proceedings of CEOS SAR Workshop*, Toulouse, France, October 26–29, 1999, 273–278 also ESASP-450 (1999), 273–278.



Lars Ulander (S'86—M'91) received the M.Sc. in engineering physics in 1985 and the Ph.D. in electrical and computer engineering in 1991, both from Chalmers University of Technology (CTH) in Göteborg, Sweden.

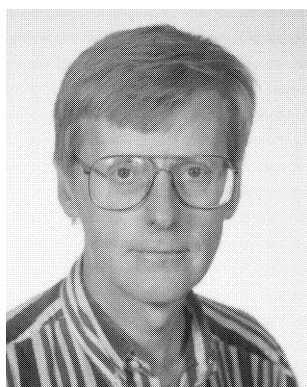
In 1995 he joined the Swedish Defence Research Agency (FOI) to work on VHF-band synthetic-aperture radar (SAR). He is currently Director of Research at FOI and also acts as Adjunct Professor in Radar Remote Sensing at CTH. His research area includes radar and electromagnetics, in particular signal processing, SAR and electromagnetic scattering. He leads the group at FOI focusing on advanced signal processing techniques for VHF- and UHF-band SAR systems, as well as implementing such techniques in airborne experimental and technology demonstrators.

Dr. Ulander is the author or coauthor of about 150 professional publications, of which more than 30 are in refereed journals. He is the holder of four patents, and is listed in *Who's Who in Electromagnetics*. He is also a member of the Remote Sensing Committee at the Swedish National Space Board.



Hans Hellsten received the Ph.D. degree from the Institute of Theoretical Physics at the University of Stockholm, Sweden, in 1980.

He joined the Swedish Defense Research Agency (FOI) in 1981. Since 1985 his professional effort has been devoted to low frequency and diffraction limited radar imaging, e.g. leading to the origination and development of the CARABAS VHF SAR. Among various research achievements, one may note the derivation of the first "exact" solution to the SAR inverse problem (together with Lars Erik Anderson). For many years Hans Hellsten headed the CARABAS development work and later the FOI Radar Surveillance Department. He is currently with Ericsson Microwave Systems and technically responsible for low frequency radar research and development within this company.



Gunnar Stenström was born in Klintehamn, Sweden, in 1951. He received the M.Sc. degree in electrical engineering from the Royal Institute of Technology, Stockholm, Sweden, in 1977. He joined the Swedish Defence Research Agency (FOI), Department of Sensor Technology, in 1977 to work with hardware and software development of a millimeter wave radar and two dual frequency millimeter wave radiometers, one of them airborne. He has carried out experiments and data analysis with the systems, measuring different environments at different times of the year. In parallel, he has worked with a high resolution coherent X-band radar and with the development of a fast radio direction finder. During 1987, he participated in an ESA feasibility study of hardware solutions to steer phased array antennas. In 1988, he joined the CARABAS project and is involved in work with hardware, digital hardware, digital software, software, and projection algorithms.